Supplemental material notes for the manuscript "Cumulative fatigue damage in thin aluminum films evaluated non-destructively with lasers via zero-group-velocity Lamb modes"

Guqi Yan, Samuel Raetz, Nikolay Chigarev, James Blondeau, Vitalyi E. Gusev, and Vincent Tournat

Laboratoire d'Acoustique de l'Université du Mans, LAUM - UMR 6613 CNRS, Le Mans Université, Avenue Olivier Messiaen, 72085 Le Mans Cedex 9, France

Supplemental Material Note 1: Details of empirically-based theoretical equations

Although it is not true in the current fatigue test since the controlled parameter is the imposed displacement of a clamped side of the plate, it is considered that the cyclic loading is strain-controlled. Therefore, the part of the theoretical damage index associated to the cumulative damage, D_c, is proposed to be modelled using the Lemaitre-Plumtree rule [1–3] that accounts for the evolution of the stress response of the material due to the material fatigue in a strain-controlled cyclic loading:

$$D_c(N,x) = \left[1 - \left(1 - \frac{N}{N_f}\right)^{1/(1+P_N)}\right] \exp\left[-4\ln 2 \frac{(x-\Delta x)^2}{\sigma^2}\right], \tag{S1.1}$$

where N_f is the number of cycles to produce a critical amount of damage (as outlined in Ref. [4]) and P_N, a dimensionless quantity, represents the damage exponent which depends on the plastic strain amplitude. Note that the value of P_N can range from one-digit number to two-digit number [3]. In Eq. (S1.1), the Lemaitre-Plumtree rule dictates the dependence of D_c on N. Assuming that the cumulative damage is concentrated in the center of the plate where the imposed fatigue stresses are the largest [see Fig. 4(c)], the spatial distribution of the effect of cumulative damage is proposed to be captured with a narrow Gaussian distribution along the scanning distance x with the parameters σ (full width at half maximum: FWHM) to control its width and Δx to control the position of its maximum. The Gaussian distribution is here taken, after experimental observations of the spatial distribution of the relative variation of the ZGV frequency (see Fig. 6) and that of the optical microscope [see inset in Fig. 7(d)]. According to the the stress distribution [see Fig. 4(c)], the extent of the damage in the center of the plate should increase quicker than that in the side parts. The Gaussian distribution width σ should thus rigorously decrease as N increases, hence concentrating the damage more and more to the center. Yet, looking at the experimental results of the distribution in Fig. 6, the Gaussian distribution width in Zone I is observed to be quasi-constant. It has thus been assumed to set σ as a constant in Eq. (S1.1).

For the other two terms of D, D_b and D_t, the Miner-linear damage hypothesis [2, 5] is considered to model their dependence on N: linear dependence of the form N/N_f. Indeed, it is assumed that the metal fatigue is weaker is Zone II and Zone III and, therefore, that the stress response evolves linearly with N. Since the buckling-caused residual stress has the form of a cosine function with respect to x [see Eq. (3)], so is the spatial distribution of D_b, which leads to the following

expression:

$$D_b(N,x) = \frac{N}{N_f}\left|\cos\left(\pi\frac{x-\Delta x}{L+\delta l}\right)\right|, \tag{S1.2}$$

where δl stands for the elongation of the specimen due to the traction (assumed to be the same for all unloading) and the absolute value accounts for the fact that, whether the loading stress is positive or negative, contributes to the damage the same way. Note that the latter is an assumption to simplify the model and barely correct since it is known that materials usually present greater yield strength in compression than in tension. The global traction applied to the plate and related to D_t is assumed to be uni-axial, implying that its effect on the plate thickness does not depend on x and therefore that:

$$D_t(N) = \frac{N}{N_f}. \tag{S1.3}$$

Supplemental Material Note 2: Details of the finite element simulations

The acoustic wave equation in its vectorial expression is written as,

$$\nabla\cdot[\mathbf{C}:(\nabla+\nabla^t)\mathbf{u}] - \rho\frac{\partial^2\mathbf{u}}{\partial t^2} = \mathbf{S}, \tag{S2.1}$$

where $\mathbf{C}$ is the 4^{th} order stiffness tensor, $\mathbf{u}$ is the displacement field, ρ stands for the density of the material, and the source term $\mathbf{S}$ in the right hand part is the gradient of the thermal stresses induced by the laser absorption, expressed as,

$$\mathbf{S} = [S_x, S_z]^{\mathbf{T}} = \nabla\cdot[\mathbf{C}:\overline{\alpha}\Delta T]. \tag{S2.2}$$

In Eq. (S2.2), $\overline{\alpha}$ is the thermal dilatation tensor. The temperature rise $T = T(x,z,t)$ could be calculated by solving the heat equation [6],

$$\rho C_p\frac{\partial T(x,z,t)}{\partial t} - \kappa\nabla^2 T(x,z,t) = \beta I_0 e^{-\beta z} f(t)G(x), \tag{S2.3}$$

where C_p is the heat capacity per unit mass of the material, $I_0 = \eta I$ is the absorbed intensity of the laser beam, β is the optical absorption coefficient, $f(t)$ is the normalized time distribution of the laser intensity and $G(x)$ is the Gaussian distribution of the normalized laser intensity expressed as,

$$G(x) = \frac{2}{d}\sqrt{\frac{\ln 2}{\pi}}\exp\left[-4\ln 2\frac{x^2}{d^2}\right],$$

with d the FWHM of the Gaussian distribution. In Eq. (S2.3), κ represents the thermal conductivity, the operator $\nabla^2 = \frac{\partial^2}{\partial x^2} + \frac{\partial^2}{\partial z^2}$ denotes the Laplacian.

TABLE S1. Mechanical, thermal and optical properties of the aluminum plate used in this work for both theoretical calculations and numerical simulations.

	Value
Young's modulus (GPa) E	70
Poisson ratio ν	0.35
Density (kg/m^3) ρ	2700
Thickness (μm) 2h	75
Pulse energy (μJ) I	70
Pulse duration (ns) τ	0.75
Pulse wavelength (nm) λ_L	1064
Pulse FWHM (μm) d	20
Absorption coefficient (%) η	6$\sim$7
Heat Capacity (J/kg·K) C_p	897
Thermal expansion (1/K) α	$2.3{\cdot}10^{-5}$
Penetration depth (nm) $1/\beta$	8.98
Thermal conductivity (W/m·K) κ	237

Noting that the optical penetration depth ($1/\beta$) is small in the case of aluminum (~ 9 nm at 1064 nm), the volume source is chosen to be replaced, in the numerical model, by a shear stress dipole with a short pulse duration, as indicated in the reference [7]. Note that all the model parameters for aluminum can be found in Tab. S1. The two-dimensional FEM model is therefore constructed in the following usual order:

1. the geometry is defined,
2. the boundary conditions are set (for instance, the shear stress dipole at the surface),
3. the mesh and mesh parameters are set,
4. the solver parameters are chosen adequately (for instance, the time step) to solve the above-described wave equation [see Eq. (S2.1) with $\mathbf{S} = \mathbf{0}$] in two dimensions.

First, the geometry of the plate is defined. The plate is chosen to be split in three parts. The central part ranges in $x = [-3.75, 3.75]$ mm and is the one from which the calculations will be used for analyzes. In order to avoid the reflections from the left and right vertical boundaries of the central part, two symmetric perfect matching layers (PML), with gradient high loss, are added to

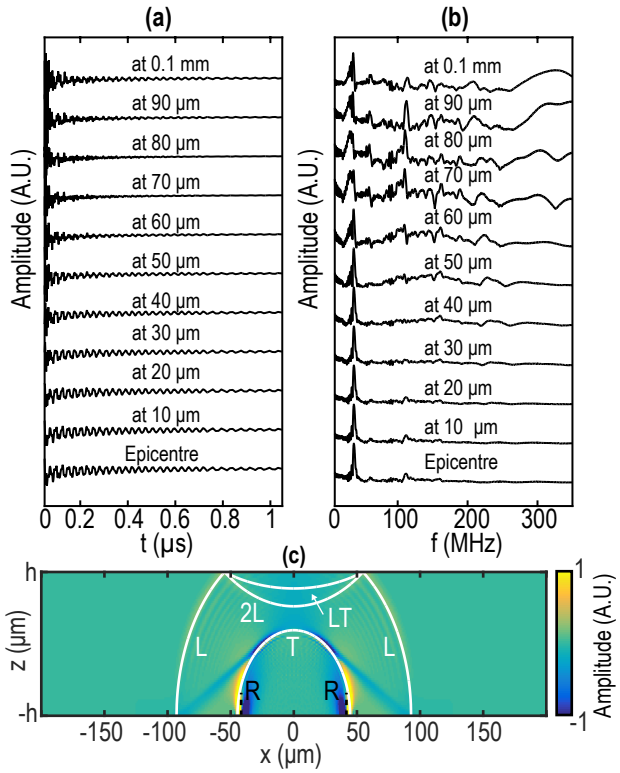

FIG. S1. Results of the numerical simulations for the intact specimen ($N = 0$) : **(a)** first eleven temporal opto-acoustic signals (normal velocity of the front surface $[z = -h]$ calculated by numerical simulations from the epicenter ($x = 0$ mm) to $x = 0.1$ mm with a step of 10 μm and **(b)** their Fourier spectrum; **(c)** zoom for $x \in [-0.20.2]$ *mm* of the spatial distribution of the normalized amplitude of the normal velocity in a 75 μm-thick aluminum plate at 15 ns after the wave generation.

the left and right ends of the model at $x = \pm 3.75$ mm. In the central part, the geometry of the plate evolves as a function of the loading cycles N. This evolution is provided by the theory proposed in Sec. 5.1 [see Eqs. (7)-(8) and Fig. 8]. For each given N, despite the changes in the geometry of the model, there are clear and uniform definitions of boundary conditions on the four sides of the modelled plate (upper, lower, left, and right surfaces). The upper and lower surfaces of the two-dimensional model are set to be free. Those upper and lower surfaces in the intact case ($N = 0$) are chosen to be flat and located at $z = +h$ and $z = -h$, respectively, with $2h = 75$ μm. In the cases of the damaged plate, the positions of the upper and lower surfaces are represented by functions of x and of N : $z_{up}(N,x) = +h[1 + D(N,x)]$ and $z_{low}(N,x) = -h[1 + D(N,x)]$, respectively (see the colored profiles in Fig. 8). The right-end surface of the right PML and the left-end surface of the left PML are set to be free, although it does not change much if they are set to be fixed. The

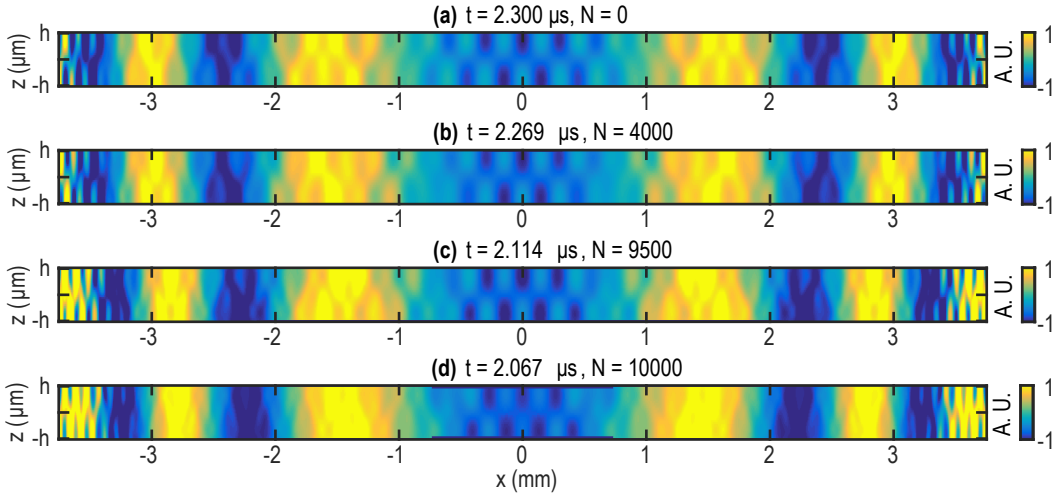

FIG. S2. Numerical simulations of the normal velocity distribution at about 90 periods, i.e. $t \cong 90/f(N)$, for intact ($N = 0$) and damaged ($N = 4000$, 9500 and 10000) specimens, taking into account the reduction of thickness as illustrated in Fig. 8.

last boundary conditions to impose is the shear stress dipole at the lower surface. The temporal distribution $f(t)$ of the generation source is a Gaussian function which can be written as

$$f(t) = \frac{2}{\tau}\sqrt{\frac{\pi}{\ln 2}}\exp\left(-4\ln 2\frac{t^2}{\tau^2}\right), \tag{S2.4}$$

where τ is the temporal pulse duration. Note that while setting f to be the temporal distribution of the acoustic source, the choice is made to calculate the velocity field instead of the displacement field, mainly for numerical stability reason.

To finish the configuration of the model, the central part of the geometry is meshed by setting the mesh geometry to be triangular and the mesh step to be 1 μm. The finite element meshes are therefore fine enough (compared to the ZGV mode wavelength, about 300 μm in the studied case) near the excited zone in order to obtain the transient velocity field with a good spatial accuracy. The PML are meshed using a much coarser mesh size of 15 μm in order to save computing time. Finally, the time step is chosen to be 1 ns (equal to the experimental acquisition time step) and the total time of the simulation is set to be 5 μs which is long enough for Fourier transform with a relative good accuracy. The simulated results by the above-described model in the case of an intact $(N = 0)$ plate of aluminum are shown in Fig. S1: (a) first eleven temporal opto-acoustic signals (normal velocity of the front surface ($z = -h$) calculated by numerical simulations from the epicenter ($x = 0$ mm) to $x = 0.1$ mm with a step of 10 μm and (b) their Fourier spectrum; (c)

zoom for $x \in [-0.2,\ 0.2]$ mm of the spatial distribution of the normalized amplitude of the normal velocity at 15 ns after the wave generation.

From Fig. S1(a), we can see clearly the temporal oscillations corresponding to the ZGV resonance in both the excitation position (x = 0) and the detected points far from it (x = 0.01, 0.02 ... 0.1 mm). An evident decrease of the amplitude of the ZGV resonance is also observed due to the spatial distribution related to the interference pattern discussed previously. From Fig. S1(b), three main pieces of information can be obtained: (i) a sharp peak, corresponding to the ZGV resonance at a frequency of about 38.42 MHz, is always observed in the frequency spectrum from the epicenter to x = 0.1 mm; (ii) a second relatively weaker peak around 62.10 MHz is also seen which corresponds to the cut-off frequency of the A_2 resonance (there is no A_2A_3-ZGV resonance in the studied case due to the chosen material with a Poisson's ratio of 0.35 [8]); (iii) a sharp peak around 125 MHz is obtained and corresponds to the S_3S_6-ZGV resonance. From Fig. S1(c), standard wavefronts of longitudinal waves (represented by L), shear waves (represented by T), and waves reflected at the back surface of the plate ($z = h$), with mode conversion (LT) or not (2L), are respectively observed. The Rayleigh waves (R in black) propagating only at the surface where the generation is achieved ($z = -h$) are also observed. All these numerical results demonstrate the good numerical reproduction of the usual features observed in laser ultrasonic experiments conducted on metals and therefore qualitatively validate the developed model. The numerical model is then run four times, each time only changing the parameter N (the number of loading cycles) and therefore the geometry of the plate: $N \in$ [0, 4000, 9500, 10000]. The Fig. S2 depicts four snapshot of the normalized normal velocity distribution within the whole range of valid calculations, where $(x,z) \in [-3.75, 3.75] \times [-0.0375, 0.0375]$ mm^2. Note that each snapshot is taken at a time corresponding to approximately 90 periods of the S_1S_2-ZGV resonance, i.e. at $t \simeq 90/f_{\mathrm{ZGV}}(N,0)$ for the sake of the comparison. In Fig. S2(a), the classical interference pattern of a ZGV resonance is seen between -1 mm and 1 mm, while the propagating modes have escaped the area of the wave generation and propagate towards the left-end and right-end of the plates with different group velocities. In Fig. S2(b)-(d) where the plate is damaged, the same observations could be made, although the spatial extend of the ZGV-related interference pattern in the central part seems to decrease as N increases. Qualitatively, this is due to the expected decrease of the ZGV wavelength with decreasing thickness of the plate.

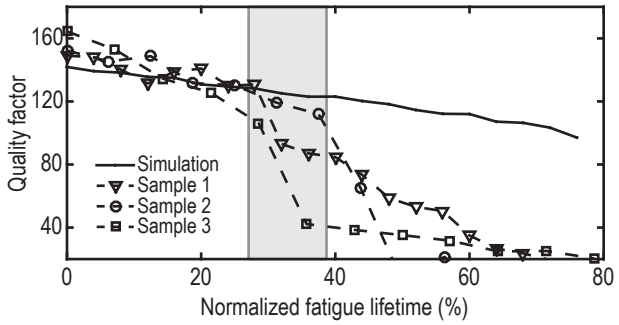

FIG. S3. The Q-factor evolutions measured in sample 1, 2, and 3 (failure at approximately 12500, 16000 and 14000 loading cycles, marked as triangles, circles, and squares) as a function of normalized fatigue lifetime, compared to the calculations of numerical simulations (solid line) from Fig. 11(b).

Supplemental Material Note 3: Discussions about the reproducibility of experiments

In this section, we discuss the reproducibility of experimental results. As mentioned in Sec. 1, the repeatability of the ZGV frequency variations has already been discussed and presented in our previously published work [9]. However, the quality factor (Q-factor) of the ZGV resonance was not discussed in this paper [9]. Therefore, in Fig. S3, we show here the comparison of the Q-factors estimated from the ZGV resonance of three aluminum samples, subjected to the same fatigue process, with failures after 12500, 16000 and 14000 loading cycles. For details of the ZGV frequency results about these three samples, please see Page 3-4 and Fig. 3 in Ref. [9]. In Fig. S3, the x-axis is normalized by the total loading cycles of each sample. The drop of the Q-factors is found to lie in the $[28\%,\ 37\%]$ interval of fatigue lifetime (see the gray area in Fig. S3). This reproducible drop of the Q factor after about 30% of the fatigue lifetime of the three samples is an experimental observation that we believe has a potential opportunity to improve the current modelling.

[1] J. Lemaitre and J. Dufailly, Eng. Fract. Mech. **28**, 643 (1987).

[2] A. Fatemi and L. Yang, Int. J. Fatigue **20**, 9 (1998).

[3] A. Plumtree and B. P. D. O'Connor, Int. J. Fatigue **11**, 249 (1989).

[4] J. Lemaitre and A. Plumtree, J. Eng. Mater. Technol. **101**, 284 (1979).

[5] M. Miner, J. Appl. Mech. **12**, A159 (1945).

[6] S. Raetz, T. Dehoux, and B. Audoin, J. Acoust. Soc. Am. **130**, 3691 (2011).

[7] C. Scruby and L. Drain, *Laser Ultrasonics Techniques and Applications* (Taylor & Francis, 1990).

[8] D. Clorennec, C. Prada, and D. Royer, J. Appl. Phys. **101**, 034908 (2007).

[9] G. Yan, S. Raetz, N. Chigarev, V. E. Gusev, and V. Tournat, Phys. Rev. Applied **9**, 061001 (2018).